Mon. Not. R. Astron. Soc. **000**, 1–18 (2012) Printed 16 January 2013 (MN LATEX style file v2.2)

Characterizing dark interactions with the halo mass accretion history and structural properties

Carlo Giocoli[1,2,3⋆], Federico Marulli[1,2,3], Marco Baldi[1], Lauro Moscardini[1,2,3], R. Benton Metcalf[1]

[1] *Dipartimento di Fisica e Astronomia, Università di Bologna, viale Berti Pichat 6/2, 40127, Bologna, Italy*
[2] *INAF - Osservatorio Astronomico di Bologna, via Ranzani 1, 40127, Bologna, Italy*
[3] *INFN - Sezione di Bologna, viale Berti Pichat 6/2, 40127, Bologna, Italy*

ABSTRACT

We study the halo mass accretion history (MAH) and its correlation with the internal structural properties in coupled dark energy cosmologies (cDE). To accurately predict all the non-linear effects caused by dark interactions, we use the COupled Dark Energy Cosmological Simulations (CoDECS). We measure the halo concentration at $z = 0$ and the number of substructures above a mass resolution threshold for each halo. Tracing the halo merging history trees back in time, following the mass of the main halo, we develope a MAH model that accurately reproduces the halo growth in term of M_{200} in the ΛCDM Universe; we then compare the MAH in different cosmological scenarios. For cDE models with a weak constant coupling, our MAH model can reproduce the simulation results, within 10% of accuracy, by suitably rescaling the normalization of the linear matter power spectrum at $z = 0$, σ_8. However, this is not the case for more complex scenarios, like the "bouncing" cDE model, for which the numerical analysis shows a rapid growth of haloes at high redshifts, that cannot be reproduced by simply rescaling the value of σ_8. Moreover, at fixed value of σ_8, cold dark matter (CDM) haloes in these cDE scenarios tend to be more concentrated and have a larger amount of substructures with respect to ΛCDM predictions. Finally, we present an accurate model that relates the halo concentration to the time at which it assembles half or 4% of its mass. Combining this with our MAH model, we show how halo concentrations change while varying only σ_8 in a ΛCDM Universe, at fixed halo mass.

Key words: galaxies: haloes - cosmology: theory - dark matter - methods: numerical

1 INTRODUCTION

Understanding the formation and evolution of structures in the Universe is one of the main goals of present cosmological studies. Following the standard scenario, the formation of cosmic structures up to protogalactic scale is due to the gravitational instability of the dark matter (DM) (Frenk et al. 1983; Davis et al. 1985; White 1988; Frenk et al. 1990; Springel et al. 2005, 2008). When a density fluctuation exceeds a certain value, it collapses forming a so-called DM halo. The small systems collapse first in a denser Universe and then merge together forming the larger ones, thereby giving rise to a hierarchical process of structure formation. In this scenario, galaxy clusters are located at the top of the merger history pyramid and today represent the largest virialized objects in the Universe. The formation of luminous objects happens when baryons, feeling the potential wells of the DM haloes, fall inside them shocking, cooling and eventually forming stars (White & Rees 1978). New supplies of gas and galaxy mergers tend to modify the dynamical and morphological properties of the forming systems, and are closely linked to the mass accretion histories of the haloes they inhabit. A detailed understanding of how this mass accretion occurs and how individual halo properties depend on their merger histories is of fundamental importance for predicting galaxy properties within the CDM theory and, similarly, for using observed galaxy properties (as e.g. rotation curves) to test the paradigm.

Different definitions have been adopted in the literature to study the halo growth along the cosmic time and its correlation with the halo clustering on large scales (Gao et al. 2004; Gao & White 2007). From different analyses it has emerged that while the redshit, z_f, at which the main halo progenitor assembles a fraction, f, of its mass correlates with its global structural properties (as e.g. its concentration, spin parameter, subhalo population, etc.), the redshift,

⋆ E-mail: carlo.giocoli@unibo.it

z_c, at which the main halo progenitor assembles a constant central mass, M_c, mainly correlates with the typical formation time of stars in a halo. Considering the haloes at $z = 0$ in the Millennium Simulation, Li et al. (2008) have shown that, while z_f decreases with the halo mass, z_c grows with it, in agreement with the fact that older stellar populations tend to reside in more massive systems.

Many studies conducted on standard ΛCDM simulations have also underlined how structural halo properties, like concentration and subhalo population, are related to the MAH (van den Bosch 2002; Gao et al. 2004, 2008). Less massive haloes, typically assembling a given fraction of their mass earlier, tend to host less substructures than the more massive ones. In particular, Giocoli et al. (2008) found that at fixed halo mass more concentrated haloes tend to possess less substructures because forming at higher redshift than the less concentrated ones. Extending these results to the framework of the assembly bias we would expect – at fixed halo mass – more concentrated, more relaxed, and less substructured haloes to be on average more biased with respect to the DM.

Analytical models of the DM density distribution, based on the halo model (Seljak 2000; Cooray & Sheth 2002; Giocoli et al. 2010), require knowledge of the halo mass function, density profile, concentration and subhalo population; as does the halo occupation distribution (HOD) approach to describe the galaxy and the quasar luminosity function and their bias (Moster et al. 2010; Shen et al. 2010; Cacciato et al. 2012). At the same time, these results are useful to model the weak and strong lensing signals by large scale structures (Bartelmann & Schneider 2001) and clusters (Giocoli et al. 2012a) in standard and non-standard cosmologies. Since many cosmological models have been proposed as a possible alternative to the standard *concordance* ΛCDM scenario, it is natural to investigate whether these results can also be extended to non-standard cosmologies. In this paper, we will focus on a range of DE scenarios characterized by a non-vanishing coupling between the DE field and CDM particles, which go under the name of cDE (Wetterich 1995; Amendola 2000, 2004).

This paper is divided in two parts. In the first part, we investigate the impact of a number of cDE models on the formation and accretion histories of CDM haloes (§2 – §5). To tackle this point, we make use of two theoretical techniques, one analytic and one numeric. The former one allows us to predict the MAH through a generalized version of the Press & Schechter (1974) formalism. The numerical approach aimed at properly describing all the non-linear effects at work. Here, we consider the mock halo catalogues extracted from the CoDECS simulations and compare them to our analytic MAH predictions. In the second part of the paper (§6), we exploit both the above theoretical methods to predict the internal structural properties of CDM haloes in these cosmological scenarios. In particular, we derive the halo concentration-mass relation, that is shown to provide a key observable to discriminate between cDE cosmologies and, in some cases, to remove the degeneracy with the normaliazion of the power spectrum.

After a general introduction to the cDE cosmologies analyzed in this work in §2, we describe our numerical N-body simulations in §3. Details on the method we use to climb the halo merging history trees are given in §4, while our theoretical predictions, both analytical and numerical, on the halo MAH are provided in §5. In §6, we investigate the halo internal structural properties. Finally, in §7 we draw our conclusions.

2 THE CDE MODELS

cDE models have been proposed as a possible alternative to the cosmological constant Λ and to standard uncoupled Quintessence models (Wetterich 1988; Ratra & Peebles 1988) to explain the observed accelerated expansion of the Universe (Riess et al. 1998; Perlmutter et al. 1999; Schmidt et al. 1998), as they alleviate some of the fine-tuning problems that characterize the latter scenarios. In order to be viable, cDE models need to assume a negligible interaction of the DE field to baryonic particles (Damour et al. 1990), since the long-range fifth-force that arises between coupled particle pairs as a consequence of the interaction with the DE field would otherwise violate solar-system constraints on scalar-tensor theories (see e.g. Bertotti et al. 2003; Will 2005). Consequently, a large number of cDE models characterized by a direct interaction between DE and CDM (see e.g. Wetterich 1995; Amendola 2000, 2004; Farrar & Peebles 2004; Caldera-Cabral et al. 2009; Koyama et al. 2009; Baldi 2011b) or massive neutrinos (see e.g. Wetterich 2007; Amendola et al. 2008) have been proposed in recent years. The basic properties of cDE models and their impact on structure formation have been thoroughly discussed in the literature. For a self-consistent introduction on cDE scenarios we suggest for example the recent reviews Tsujikawa (2010); De Felice & Tsujikawa (2010); Amendola et al. (2012, - Section 1.4.3). For the aims of the present work, it is sufficient to summarize the main features that characterize cDE models in general, and the specific realizations of the cDE scenario that will be investigated here.

In general, cDE models are characterized by two free functions that fully determine the background evolution of the Universe and the linear and non-linear growth of density perturbations. These are the self-interaction potential $V(\phi)$ and the coupling function $\beta(\phi)$, where ϕ is a classical scalar field playing the role of the cosmic DE. The coupling function $\beta(\phi)$ determines the strength of the interaction between DE and CDM (in the case investigated here) and directly affects the evolution of density perturbations through: i) a long-range attractive fifth-force of order β^2 times the gravitational strength, and ii) a velocity-dependent acceleration on coupled CDM particles proportional to $\dot{\phi}\beta$ (see e.g. Baldi 2011a). Differently from the fifth-force term, which is always attractive regardless of the sign of the coupling function and of the dynamical evolution of the DE scalar field, the friction term can take both positive and negative signs depending on the relative signs of the scalar field velocity $\dot{\phi}$ and the coupling function $\beta(\phi)$. Such feature can have very significant consequences on the evolution of structure formation in case the friction term changes sign during the cosmic evolution (Baldi 2012a; Tarrant et al. 2012) as for the case of the "bouncing" cDE model (Baldi 2012a) investigated in this work.

Table 1. The cDE models of the CoDECS suite considered in the present work. All models have the same normalization of scalar perturbations at $z_{\rm CMB} \approx 1100$ leading to a different value of σ_8. Besides σ_8 and the value of the DE equation of state w_ϕ all the models share the same WMAP7 (Komatsu et al. 2011) cosmological parameters at the present time.

Model	Potential	α	β_0	β_1	Scalar field normalization	Potential normalization	$w_\phi(z=0)$	$\mathcal{A}_s(z_{\rm CMB})$	$\sigma_8(z=0)$
ΛCDM	$V(\phi) = A$	–	–	–	–	$A = 0.0219$	-1.0	2.42×10^{-9}	0.809
EXP003	$V(\phi) = Ae^{-\alpha\phi}$	0.08	0.15	0	$\phi(z=0) = 0$	$A = 0.0218$	-0.992	2.42×10^{-9}	0.967
EXP008e3	$V(\phi) = Ae^{-\alpha\phi}$	0.08	0.4	3	$\phi(z=0) = 0$	$A = 0.0217$	-0.982	2.42×10^{-9}	0.895
SUGRA003	$V(\phi) = A\phi^{-\alpha}e^{\phi^2/2}$	2.15	-0.15	0	$\phi(z\to\infty) = \sqrt{\alpha}$	$A = 0.0202$	-0.901	2.42×10^{-9}	0.806

3 NUMERICAL SIMULATIONS

We make use of the public halo and subhalo catalogues of the CoDECS[1] simulations (Baldi 2012b) – the largest suite of cosmological N-body simulations of cDE models to date – to follow the accretion histories of CDM haloes by building the full merger trees of all the structures identified at $z = 0$ up to $z = 60$. In our analysis, we will consider the different combinations of the potential and coupling functions that are available within the CoDECS suite of cDE scenarios, defined by the following general expressions:

- *Exponential potential* (Lucchin & Matarrese 1985; Wetterich 1988):

$$V(\phi) = Ae^{-\alpha\phi}\,; \tag{1}$$

- *SUGRA potential* (Brax & Martin 1999):

$$V(\phi) = A\phi^{-\alpha}e^{\phi^2/2}\,; \tag{2}$$

- *Constant coupling* (Wetterich 1995; Amendola 2000):

$$\beta(\phi) = \beta_0 = \text{const.}\,; \tag{3}$$

- *Time-dependent coupling* (Amendola 2004; Baldi 2011b):

$$\beta(\phi) = \beta_0 e^{\beta_1\phi}\,. \tag{4}$$

In particular, while standard cDE models are characterized by "runaway" potentials (like e.g. the exponential potential of Eq. 1) and a constant coupling, time-dependent cDE models feature the same type of potentials with a coupling function that evolves with the scalar field itself. Finally, the combination of a "confining" potential like the SUGRA potential of Eq. 2 with a negative constant coupling characterizes the so-called "bouncing" cDE scenario (Baldi 2012a). A summary of the cDE models that are investigated in the present work, with the corresponding parameters, is given in Table 1. For such scenarios, we will make use of the publicly-available data of the L-CoDECS series to derive halo accretion histories in the different cosmologies.

The L-CoDECS runs are collisionless N-body simulations carried out on a periodic cosmological box of 1 Gpc/h aside, filled with 2×1024^3 equally sampling the coupled CDM and the uncoupled baryon fluids. The baryons are treated as a separate family of collisionless particles, and no hydrodynamic treatment is included in the simulations. The mass resolution at $z = 0$ is $m_c = 5.84 \times 10^{10}$ M$_\odot/h$ and $m_b = 1.17 \times 10^{10}$ M$_\odot/h$ for CDM and baryon particles, respectively, while the gravitational softening is $\epsilon_g = 20$ kpc/h. All the models virtually share the same initial conditions at the redshift of last scattering $z_{\rm ls} \approx 1100$ and are consequently characterized by a different value of σ_8, due to their different growth histories (as summarized in Table 1). Except for the different values of σ_8 and of the DE equation of state parameter w_ϕ, all the models share the same cosmological parameters at $z = 0$, consistent with the WMAP7 results (Komatsu et al. (2011), see Table 2). This provides a self-consistent set of cosmologies that can be directly compared with each other and tested with present and future observations. The viability of these models in terms of CMB observables has yet to be properly investigated, in particular for what concerns the impact of variable-coupling and "bouncing" cDE models on the large-scale power of CMB anisotropies. Although such analysis might possibly lead to tighter bounds on the coupling and on the potential functions than the ones allowed in the present work, here we are mainly interested in qualitatively understanding the impact of cDE scenarios on the formation history of CDM haloes at late times, and we deliberately choose quite extreme values of the models parameters in order to maximize the effects under investigation.

The CoDECS simulations have already been used for several investigations. In particular, Lee & Baldi (2011) exploited these data to study the pairwise infall velocity of colliding galaxy clusters in cDE models, demonstrating that DE interactions can significantly enhance the probability of high-velocity collisions. Beynon et al. (2012) provided forecasts for the weak lensing constraining power of future galaxy surveys, while Cui et al. (2012) exploited the same data to test the universality of the halo mass function. Finally, the CoDECS data have been used to study how DE interactions modify the halo clustering, bias and redshift-space distortions (Marulli et al. 2012), and how they can shift the baryonic acoustic oscillations (Vera Cervantes et al. 2012).

4 THE HALO MERGER HISTORY TREE

For each simulation snapshot, we identify haloes on the fly by means of a Fried-of-Friend (FoF) algorithm with linking parameter $b = 0.2$ times the mean interparticle separation. Within each FoF group we also identify gravitationally bound substructures using the SUBFIND algorithm (Springel et al. 2001b). SUBFIND searches for overdense regions within a FoF group using a local SPH density estimate, identifying

[1] www.marcobaldi.it/CoDECS

Table 2. The set of cosmological parameters assumed for all the models included in the CoDECS Project, consistent with the 7 year results of the WMAP collaboration for CMB data alone (Komatsu et al. 2011).

Parameter	Value
H_0	70.3 km s^{-1} Mpc^{-1}
$\Omega_{\rm CDM}$	0.226
$\Omega_{\rm DE}$	0.729
σ_8	0.809
Ω_b	0.0451
n_s	0.966

substructure candidates as regions bounded by an isodensity surface that crosses a saddle point of the density field, and testing that these possible substructures are physically bound with an iterative unbinding procedure. For both FoF and SUBFIND catalogues we select and store systems with more than 20 particles, and define their centres as the position of the particle with the minimum gravitational potential. It is worth to notice that while the subhaloes have a well defined mass that is the sum of the mass of all particles belonging to them, different mass definitions are associated to the FoF groups (Lukić et al. 2009). We define as M_{FoF} the sum of the masses of all particles belonging to the FoF group, M_{200} the mass around the FoF center enclosing a density that is 200 times the critical one, and M_{vir} as the one enclosing the virial overdensity Δ_{vir}, as predicted by the spherical collapse model. We notice that in the ΛCDM Universe at $z = 0$ generally it is true that $M_{200} < M_{vir} < M_{FoF}$ (Eke et al. 1996; Bryan & Norman 1998).

It is interesting to notice that the definition of M_{vir} is cosmology dependent, since it is related to the Δ_{vir} definition derived from the spherical collapse model. Generally this quantity is not directly obtainable for any arbitrary DM and dark energy model. For example, Pace et al. (2010) have shown how to compute Δ_{vir} from the non-linear differential equation for the evolution of the density contrast for dynamical and early DE cosmologies. For ΛCDM models many fitting functions are available that depend on the redshift evolution of the DM content in the Universe (Navarro et al. 1997; Bryan & Norman 1998), while no simple formulae exist Δ_{vir} within the cDE models investigated in this work. Since M_{200} is cosmology independent, we will adopt this mass definition in what follows.

For each subhalo, starting from redshift $z = 0$, we follow back its merger history tree by requiring to have at least one descended subhalo at the previous snapshot (Boylan-Kolchin et al. 2009). In order to trace back in time the growth in terms of M_{200}, we consider only *the dominant subhalo* of each FoF group to which is associated the value of M_{200} of the group. In this process we link together among the different simulation snapshots the main progenitor, defined as *the dominant subhalo* that donate the largest number of particles between two consecutive snapshots and *the satellites* that represent the progenitor haloes accreted onto the main progenitor branch of the tree (Tormen et al. 2004).

5 THE MASS ACCRETION HISTORY

Before introduce the results of the other cDE models, in this section, we review the model of the mass accretion history proposed by Giocoli et al. (2012b) for a ΛCDM model and modify it to be consistent with the M_{200} halo mass definition. This simple model allows us to derive the generalized formation redshift distribution, defined as the redshift at which the main halo progenitor assembles a fraction f of its M_{200} mass at $z = 0$, or more in general at any considered redshift z_0. Then, from such distribution we can compute the halo mass accretion history. Since haloes form as a consequence of gravitational instability processes that start within the initial DM density field and then grow together via merging events, a few important consequences are: (i) the MAH depends on the initial density fluctuation field – and so on the initial matter power spectrum; (ii) it also depends on cosmology through the background expansion of the Universe, (iii) at a given redshift more massive haloes grow faster – since they sit on the highest peaks of the density fluctuation field; (iv) at a given mass, the higher the redshift is the higher the halo mass growth rate is. These points will become more clear along the discussion of the results presented in the following sections.

5.1 Mass Accretion History in a ΛCDM Universe: revisiting the Giocoli et al. (2012b) model for M_{200}

Giocoli et al. (2012b) developed a simple and accurate model to describe the growth of CDM haloes along cosmic time. Their study was conducted analyzing the merger trees extracted from a cosmological N-body simulation of a ΛCDM Universe, the GIF2 simulation (Gao et al. 2004; Giocoli et al. 2008, 2010a).

Before describing the model, let us first introduce some universal quantities that will be used throughout this work. We define $S(M)$ as the variance of linear fluctuation field when smoothed with a top-hat filter on a scale $R = (3M/4\pi\bar{\rho})^{1/3}$:

$$S(M) = \frac{1}{2\pi^2}\int_0^R W^2(kR)P_{lin}(k)k^2{\rm d}k\,, \qquad (5)$$

where $\bar{\rho}$ is the comoving density of the background, $P(k)_{lin}$ the linear matter power spectrum and $W(kR)$ the top-hat window function. We also define $\delta_c(z)$ as the initial overdensity required for spherical collapse at redshift z:

$$\delta_c(z) = \frac{\delta_{c,lin}(z)}{D_+(z)}\,, \qquad (6)$$

where $\delta_{c,lin}(z)$ is the linear overdensity at redshift z and $D_+(z)$ the growth factor normalized to unity at the present time. For a CDM Universe, Nakamura & Suto (1997) have presented a useful fitting function for the linear overdensity as a function of the matter density parameter, Ω_m, that can be read as:

$$\delta_{c,lin}(z) = 1.686[1 + 0.123\log(\Omega_m(z)] \qquad (7)$$

and that will be used throughout this paper. In Figure 1 we show the mass variance for the four cosmological models considered in this work. We notice that all of them have the same shape but a different normalization. This is due to the

different values of σ_8 defining the variance of linear density fluctuations on a scale of 8 Mpc/h:

$$\sigma_8^2(M) = \frac{1}{2\pi^2}\int_0^8 W^2(8k)P_{lin}(k)k^2\mathrm{d}k\,; \qquad (8)$$

the higher is σ_8 the higher the normalization of the mass variance and viceversa.

Following the formalism by Lacey & Cole (1993), we can define the formation redshift z_f of a halo of mass M (at redshift z_0) as the redshift at which the main halo progenitor assembles for the first time half of its mass. Their proposed redshift distribution at half-mass, in terms of universal variables, can be read as:

$$p(w_f) = 2w_f\,\mathrm{erfc}\left(\frac{w_f}{\sqrt{2}}\right), \qquad (9)$$

where $w_f = (\delta_c(z_0) - \delta_c(z_f))/\sqrt{S(M/2) - S(M)}$. It is interesting to notice that written in this way the formation redshift distribution is both independent of the halo mass M and of the redshift z_0. In a more general way Nusser & Sheth (1999) have developed a formalism to describe the redshift at which the main halo progenitor assembles a fraction $1/2 \leqslant f < 1$ of its mass, that is:

$$p(w_f) = 2w_f\left(\frac{1}{f}-1\right)\mathrm{erfc}\left(\frac{w_f}{\sqrt{2}}\right)+\left(2-\frac{1}{f}\right)\sqrt{\frac{2}{\pi}}\exp\left(-\frac{w_f^2}{2}\right), \qquad (10)$$

which for $f = 1/2$ gives back the above expression (9). However, comparing these distributions with measurements performed on numerical simulations, Giocoli et al. (2007) have shown that they tend to underestimate the formation redshift distribution. To reconcile theory and simulations they proposed to modify $w_f \to \sqrt{0.707}w_f$ in the context of the ellipsoidal collapse model (Sheth & Tormen 1999, 2002; Despali et al. 2012). Giocoli et al. (2012b) have shown that in numerical simulations the modified equation (10) works quite well for smaller values of f. They also provided a new function to describe the formation redshift distribution for any fraction $0 < f < 1$:

$$p(w_f) = \frac{\alpha_f w \mathrm{e}^{w^2/2}}{\left[\mathrm{e}^{w^2/2} + \alpha_f - 1\right]^2}, \qquad (11)$$

where α_f represents a free parameter. By integrating Eq. 11 one gets the following cumulative generalized formation redshift distribution:

$$P(> w_f) = \frac{\alpha_f}{\mathrm{e}^{w_f^2/2} + \alpha_f - 1}. \qquad (12)$$

Since the previous equation can be inverted, it is possible to analytically compute the median value $w_f = \tilde{w}_f$ given by definition when $P(> \tilde{w}_f) = 1/2$; this gives the median redshift $z_f = \delta_c^{-1}(z_f)$ at which the main halo progenitor assembles a fraction f of its mass M:

$$z_f: \quad \delta_c(z_f) = \delta_c(z_0) + \tilde{w}_f\sqrt{S(fM) - S(M)}\,, \qquad (13)$$

where

$$\tilde{w}_f = \sqrt{2\,\ln\left(\alpha_f + 1\right)}\,. \qquad (14)$$

In Figure 2 we show the cumulative generalized formation redshift distribution in terms of the rescaled variable w_f when the main halo progenitors assemble 90%, 50%, 10% and 1% of their M_{200} mass at $z = 0$. The data

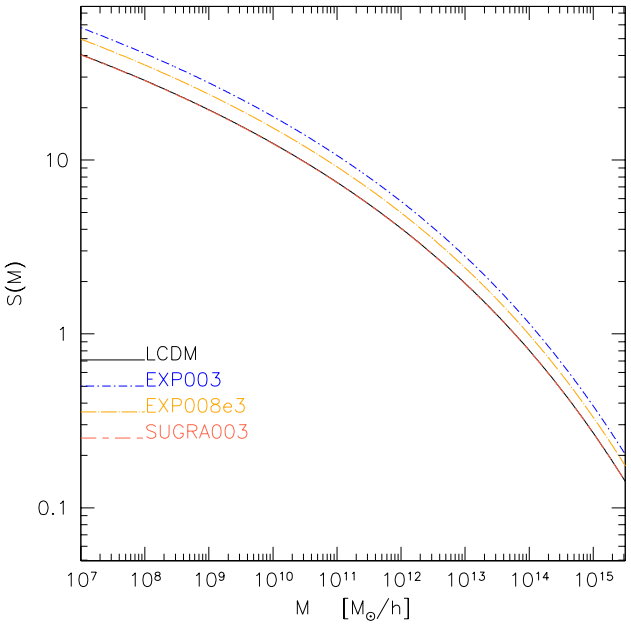

Figure 1. The mass variance S (see equation 5) as a function of the halo mass. The different curves show the results for the different linear power spectra of the models considered in this work. Their shapes are independent of the cosmological model considered while the normalizations change depending on the linear power spectrum normalization and so on the corresponding σ_8.

points represent the measurements in the ΛCDM simulation considering all haloes at $z_0 = 0$ with mass larger than $M_{200} > 5 \times 10^{12} M_\odot/h$ (which means that systems are resolved with at least 40 particles) and that never exceed along their growth histories more than 10% of their mass at the present time. This ensures to consider only haloes that grow mainly hierarchically and do not fragment as a consequence of violent merging events. With respect to Giocoli et al. (2012b), in this case haloes are followed back in time considering M_{200} as mass definition instead of M_{vir} The solid curves show the best-fit model of Eq. (12), while the dashed curves represent equation (10) modified as suggested by Giocoli et al. (2007).

From the figure we notice that – since at $z = 0$ the value of M_{200} is smaller than that of M_{vir} – following the merger tree back in time in terms of M_{200} results in a value of z_f typically higher than that obtained by following back the tree in terms of M_{vir} (see Giocoli et al. 2012b, or the Appendix A where we show the same cumulative distribution of formation redshift following the haloes in term of their virial mass for the ΛCDM run).

In Figure 3 we show the best fit α_f as a function of f. The open circles show the best fit to the ΛCDM simulation measurement for different values of the assembled mass fraction, while the solid line refers to the best fit to the data given by:

$$\alpha_f = \frac{1.365}{f^{0.65}}\,\mathrm{e}^{-2f^3}. \qquad (15)$$

Finally, the shaded regions represent the 1σ and 2σ contours of $\Delta\chi^2$, where $\chi^2(\alpha_f) = \sum_i [P_i - P(> w_{i,f}, \alpha_f)^2]$.

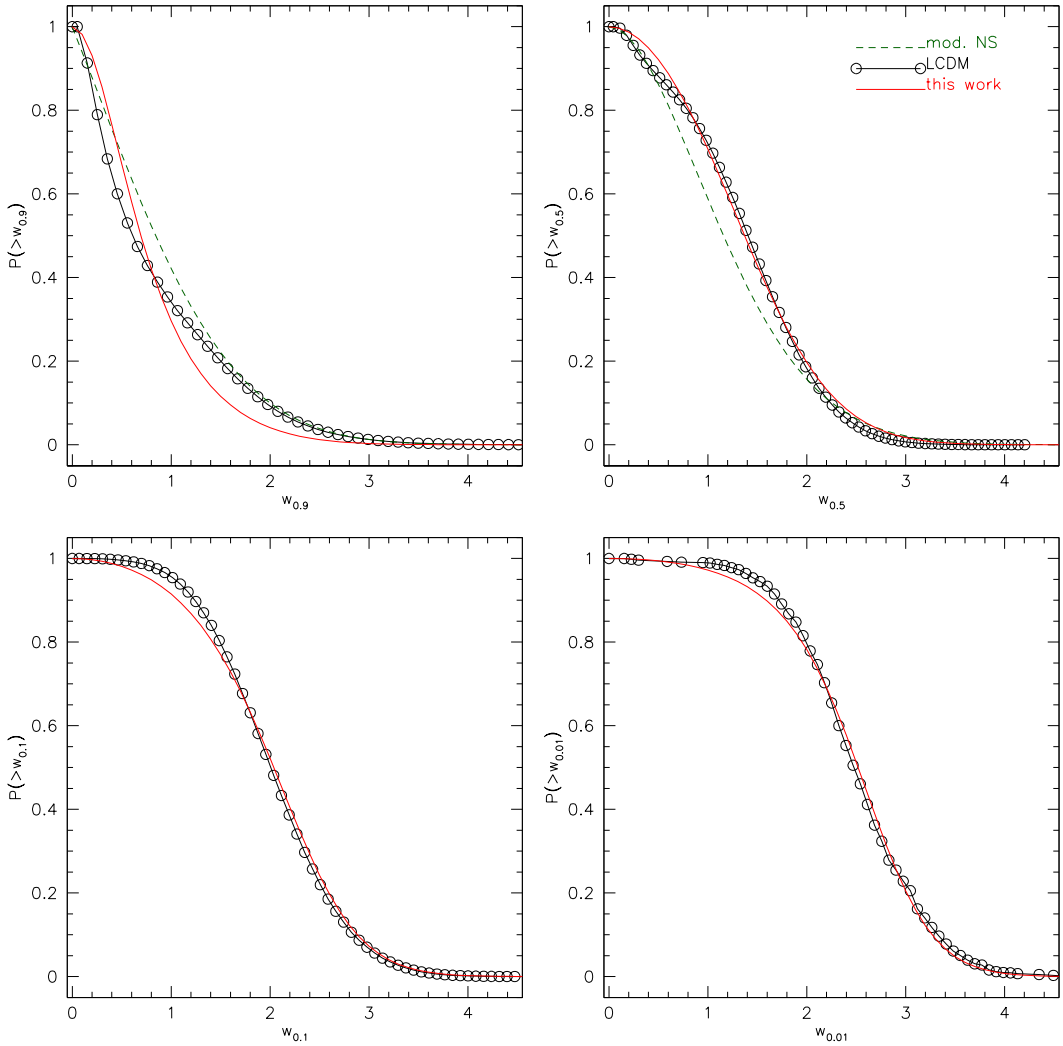

Figure 2. Cumulative generalized formation distribution, as a function of w_f, when the main halo progenitor assembles 90% (top-left panel), 50% (top-right panel), 10% (bottom-left panel) and 1% (bottom-right panel) of its M_{200} mass at redshift zero. The data points show the measurements for the ΛCDM simulation considering all haloes with at least 40 particles. The dashed curve on the top panels refers to the model by Nusser & Sheth (1999) – valid only for $1/2 < f \leqslant 1$, while the solid curve represents eq. (12) with the best fit parameter α_f. We recall that we consider only haloes that along their growth never exceed more than 10% their mass at the present time.

5.2 Generalized Formation Redshift and Mass Accretion History

The hierarchical model predicts that small haloes tend to form at higher redshift and then merge together forming the larger ones. The halo collapse happens when a density fluctuation exceeds the critical value predicted by the spherical collapse model. Typically, within a ΛCDM Universe fluctuations in a density field with a larger amplitude collapse earlier. This can be rephrased considering two identical CDM initial density fields but with different normalization parameters σ_8: haloes in the Universe with higher σ_8 will collapse earlier than those in the Universe with lower σ_8. This also results in the fact of same mass haloes being more concentrated in a Universe with a larger value of σ_8 (Macciò et al. 2008). In what follows we will try to understand if this holds also for different cosmological scenarios, i.e. if the mass accretion history measured in numerical simulations of cDE can be reproduced by the MAH model built for ΛCDM only by suitably changing the linear power spectrum normalization σ_8 only.

In the top panels of Figure 4 we show the median formation redshift as a function of the halo mass, considering $f = 0.9, 0.5, 0.1, 0.01$ as assembled mass fractions. The open circles show the median of the measurements in the ΛCDM simulation and the shaded region encloses the first and the third quartiles of the distribution at fixed halo mass. On average a present-day cluster size halo with mass of $10^{14} M_{\odot}/h$ assembles 90% of its mass at $z = 0.2$, 50% at 0.7 and 1% at approximately $z = 4$. The data points in the bottom panels represent the differences of the median measured in the three cDE models with respect to the ΛCDM one. In each panel, the three curves show the model of the $z_f - M_{200}$ relation rescaled with respect to the ΛCDM model computed using the formalism described in the previous section.

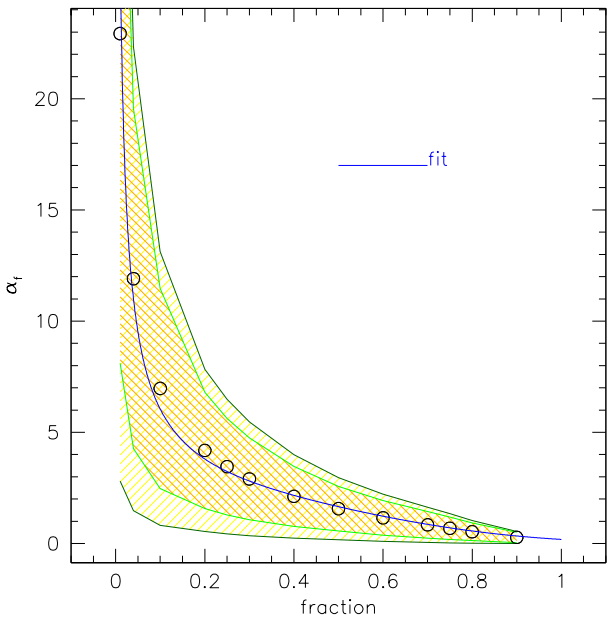

Figure 3. Dependence of α_f, the free parameter in equation (12), on the mass fraction $f = M_{200}(z_f)/M_{200}(0)$ assumed at the formation. The shaded regions represent the 1σ and 2σ contours. The blue curve represent the best fit relation.

It is important to underline that in order to build the MAH model in the three cDE cosmologies we need to know the initial density fluctuation field to compute $S(M)$, and the redshift evolution and the growth of the perturbations given by $\delta_c(z)$ and $\Delta_+(z)$. For the definition of $S(M)$, we use for the three cDE models their corresponding linear power spectra, that are obtained from the ΛCDM one by renormalizing the latter adopting the different values of σ_8 characterizing each cDE model (see Table 1). Since the purpose of this work is to understand if the MAH of the cDE simulations can be obtained from the ΛCDM by rescaling σ_8 only, we adopt for the definitions of both $\delta_c(z)$ and D_+ the ones obtained for the latter model. From Fig. 4, we notice that only for $f = 0.5$ the three cDE results are quite in agreement with the MAH model where the power spectrum normalization changes. Among them, since the SUGRA003 model has the same σ_8 of ΛCDM, we would expect to find a formation-redshift relation quite similar to the latter. However, this is clearly not the case due to the markedly different growth of SUGRA003 as compared to ΛCDM. For $f = 0.9$ and $f = 0.5$ haloes in the SUGRA003 model form typically at the same redshift as in the ΛCDM run, while for $f = 0.1$ and 0.01 the difference appears of the order of 10%. We underline also that for the two models EXP003 and EXP008e3 the halo formation redshifts are higher for any f than those measured in ΛCDM for the same mass haloes at $z = 0$.

To better understand how on average haloes assemble as a function of redshift, we show in Figure 5 the median mass accretion history for three different mass bins at $z = 0$ by defining Ψ as the logarithm of the final assembled mass fraction:

$$\Psi(z) = \log\left[\frac{M_{200}(z)}{M_{200}(0)}\right] = \log(f)\,. \qquad (16)$$

In the top panels we show the measurements for three different final halo mass bins at the present time in the ΛCDM simulation. The shaded region encloses the first and the third quartiles of the distribution at fixed halo mass fraction. The solid curve represents the model built using equation (13) for different values of the assembled halo mass fraction $0 < f < 1$.

The model predicts for the ΛCDM run a MAH that is in agreement within a few percent with the numerical simulation measurements both down to very small values of the assembled mass fraction and up to high redshifts. In the bottom panels we show the percentage difference of the MAH measured in EXP003, EXP008e3 and SUGRA003 with respect to the one in ΛCDM. In the figure, the different data points are the same as in Figure 4. The three solid curves represent the difference of MAH models changing the linear power spectrum definition with respect to the ΛCDM model. As expected, since the SUGRA003 model has almost the same linear power spectrum normalization of the ΛCDM, the MAH model predicts the same growth of the latter, in contrast with what is measured in the numerical simulation. For EXP003 the halo growth is quite well captured changing the linear power spectrum normalization in our model - and is therefore fully degenerate with σ_8. However, for EXP008e3 the model fails for large haloes and high redshift. This can be better seen in Figure 6 where we show the residuals of the MAH measured in the three cDE simulations with respect to the MAH model obtained from equation (13) changing the power spectrum normalization accordingly. The vertical dashed line in each panel shows the redshift at which the mass accretion history model falls below $5 \times 10^{12} M_\odot/h$, mass above which haloes are resolved in the simulations with at least 40 particles.

6 THE HALO STRUCTURAL PROPERTIES

6.1 Halo concentrations

One of the most important result obtained through N-body simulations of structure formation is that the CDM density distribution in collapsed haloes tends to follow a universal profile. Both for small and large mass haloes the density profile is well described by the Navarro-Frenk-White (NFW, Navarro et al. 1997) relation that reads as:

$$\rho(x) = \frac{\rho_s}{x(1+x)^2}\,, \qquad (17)$$

where $x \equiv r/r_s$, $r_s \equiv R_{200}/c_{200}$ is the scale radius where the logarithmic slope of the density profile approaches to -2, ρ_s is the density enclosed within the scale radius, and c_{200} is the halo concentration parameter. Denoting with M_{200} the mass enclosed within R_{200} we can write:

$$\rho_s = \frac{M_{200}}{4\pi r_s^3}\left[\ln(1+c_{200}) - \frac{c_{200}}{1+c_{200}}\right]^{-1}\,. \qquad (18)$$

To characterize the halo concentration in the numerical simulations we use the same approach adopted by Springel et al. (2008) and Cui et al. (2012): defining V_{max} as the maximum circular velocity of a halo and r_{max} as the radius

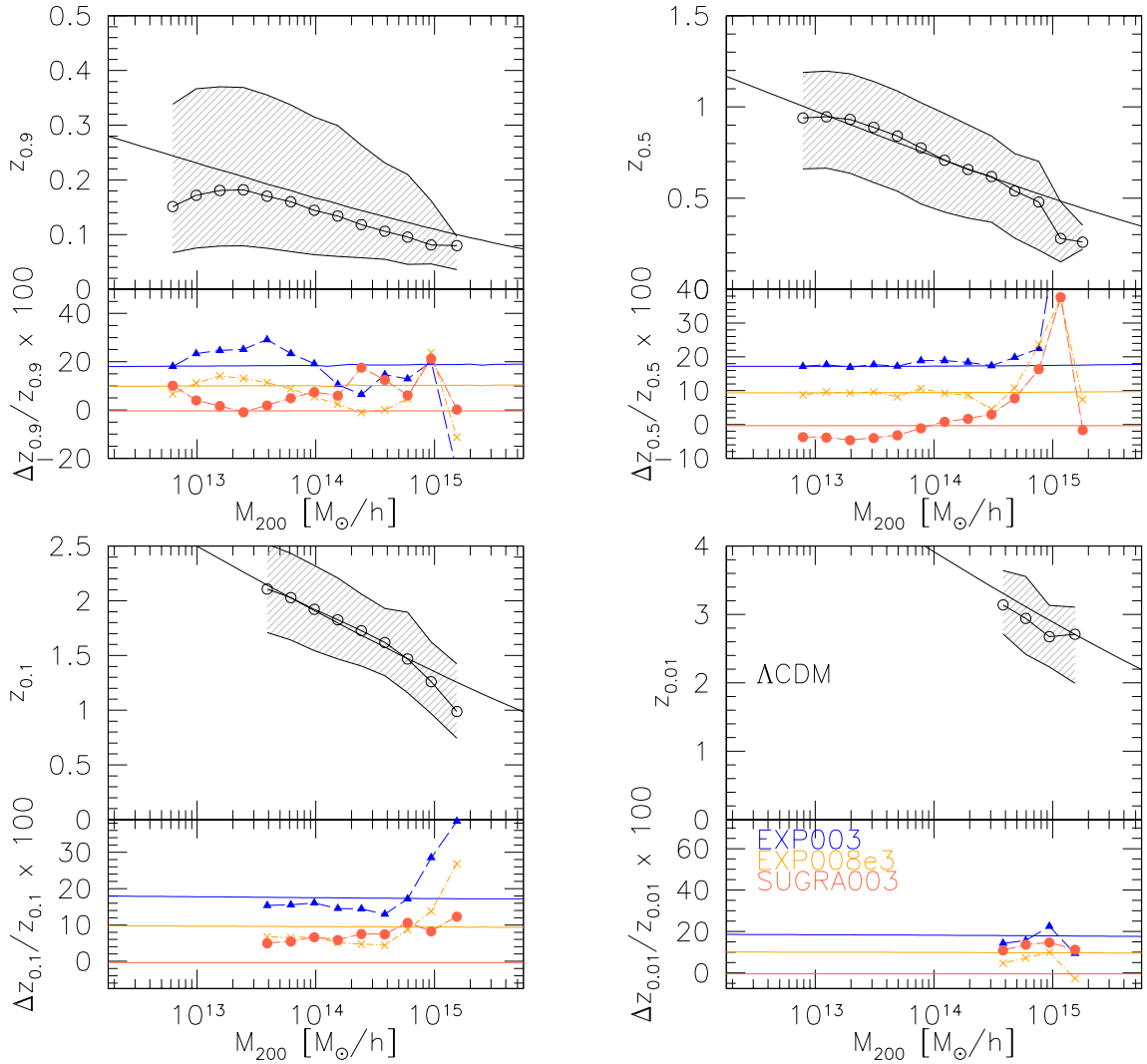

Figure 4. Top panels: median formation redshift-mass relation for haloes identified at $z_0 = 0$ in the ΛCDM simulation. The shaded region encloses the quartiles of the distribution at fixed halo mass. The solid line represents the prediction derived using the modified version of the Giocoli et al. (2012b) mass accretion history model. Bottom panels: differences with respect to the ΛCDM model for the three cDE models. The lines represent the predictions obtained from the modified model by Giocoli et al. (2012b) by changing the definition of $S(M)$ for each cosmology only.

at which this velocity is attained so we can write:

$$\frac{\rho_s}{\rho_{crit}} = \frac{200}{3}\frac{c_{200}^3}{\ln(1+c_{200}) - c_{200}/(1+c_{200})} = 14.426\left(\frac{V_{max}}{H(z)\,r_{max}}\right)^2, \quad (19)$$

where ρ_{crit} represents the critical density of the Universe. In Figure 7 we show the distribution function of the maximum circular velocity and of the radius at which it is attained for all haloes that at the present time are more massive than $5 \times 10^{13} M_\odot/h$. Since to faithfully determine the halo concentration a minimum number of particles is required (Neto et al. 2007), for this analysis we consider only haloes more massive than $5 \times 10^{13} M_\odot/h$; this lower limit ensures that the haloes are resolved with at least 850 particles. We notice that while the haloes in EXP003 and EXP008e3 have values of V_{max} and R_{max} that are not much different from the corresponding haloes in the ΛCDM, the haloes in SUGRA003 are more compact and typically have a higher maximum circular velocity that is attained at a smaller radius than in ΛCDM; as we will see later on, this corresponds to more concentrated haloes in SUGRA003 at $z = 0$ than in the other three cosmological models.

In the context of the CDM hierarchical structure formation scenario, halo concentrations are thought to be reminiscent of the cosmic mean density at the time of collapse, thereby resulting in smaller objects having on average higher concentrations due to their earlier formation epoch. Consistently with this picture, clusters of galaxies have the lowest concentrations – typically of the order of ~ 4 – being the last collapsed structures in the Universe. At fixed redshift and halo mass the concentration tends to be larger for haloes that assemble their mass earlier; this also corresponds to haloes that are, on average, more relaxed. Neto et al. (2007), Macciò et al. (2007, 2008) and De Boni et al. (2012) have shown that including unrelaxed haloes in the sample results

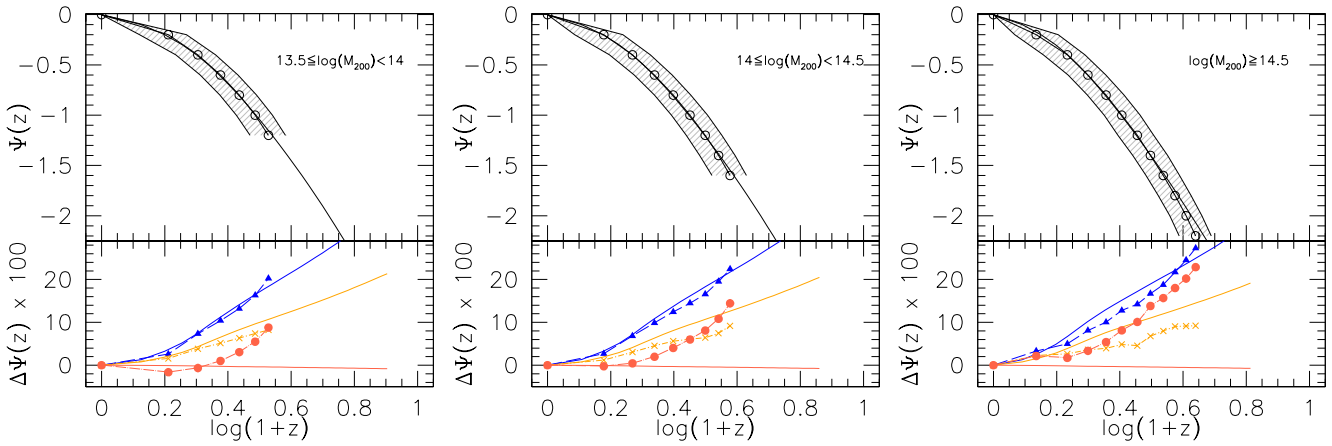

Figure 5. Median mass accretion history of main halo progenitors. In the top part of each panel we show the results from the ΛCDM simulation for three different initial mass bins, where the shaded region encloses the quartiles of the distribution at fixed halo mass fraction assembled. In each panel, the solid curve represents the prediction from eq. (13). The bottom part of each panel shows the residuals with respect to the ΛCDM simulation measurements of the three cDE models together with the residuals for the theoretical predictions changing $S(M)$ in the mass accretion history model. Point style as in Figure 4.

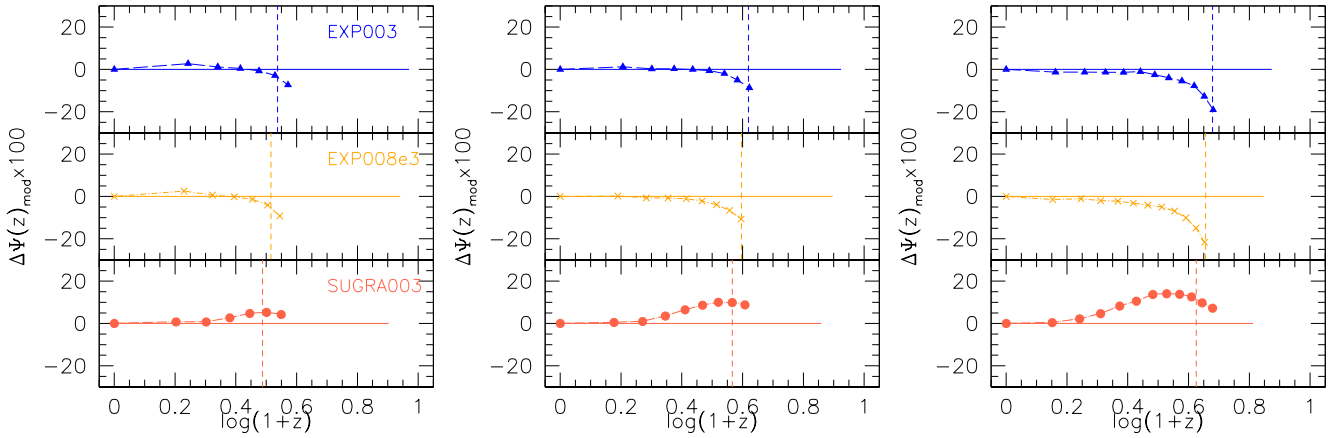

Figure 6. Residuals of the MAH measured in the three cDE models with respect to the MAH model changing the linear power spectrum normalization accordingly. The vertical dashed line in each panel shows the redshift at which the MAH model falls below the mass resolution equal to $5 \times 10^{12} M_{\odot}/h$.

in a $c - M$ relation with a lower normalization and a larger scatter.

Several studies based on the analysis of numerical simulations have shown that halo structural properties are mainly related to the halo mass accretion history, and so to their environment (Gao et al. 2004; Sheth & Tormen 2004; Gao et al. 2008). Not only do less massive haloes possess a higher concentration but typically also a smaller mass fraction in substructures (De Lucia et al. 2004; van den Bosch et al. 2005; Giocoli et al. 2010a). In particular, the $c - M$ models by Navarro et al. (1997) and Bullock et al. (2001) rely on the idea that the central density of the haloes reflects the mean density of the Universe at a time when the central region of the halo was accreting matter at a high rate. In this framework Zhao et al. (2009) define this epoch when the main halo progenitor is assembling 4% of its final mass.

In order to understand how halo concentration correlates with the accretion history, in what follows we study the correlation between c_{200} and two conventional markers of the halo MAH: $z_{0.5}$ i.e. the redshift at which the main halo progenitor assembles half of its final mass (we will denote with $t_{0.5}$ the corresponding cosmic time) and $z_{0.04}$ (at which corresponds $t_{0.04}$), i.e. the redshift at which it assembles 4% of its mass.

In Figure 8 we show the correlation between the halo concentration and $t_0/t_{0.5}$ where t_0 represents the time at which the halo is considered – in our case $z_0 = 0$. In each panel we show the measurements for all haloes more massive than $5 \times 10^{13} M_{\odot}/h$ in the ΛCDM and the three cDE models. The data points with error bars show the median of the correlation and the quartiles of the distribution at fixed $t_0/t_{0.5}$. In the top-left panel the solid black line shows the least-square fit to the ΛCDM measurements, and the dotted red curve represents the following best-fit power law-relation obtained by minimizing the scatter:

$$c_{200} = 4 \left[1 + \left(\frac{t_0}{1.5 t_{0.5}} \right)^{5.2} \right]^{1/5} . \qquad (20)$$

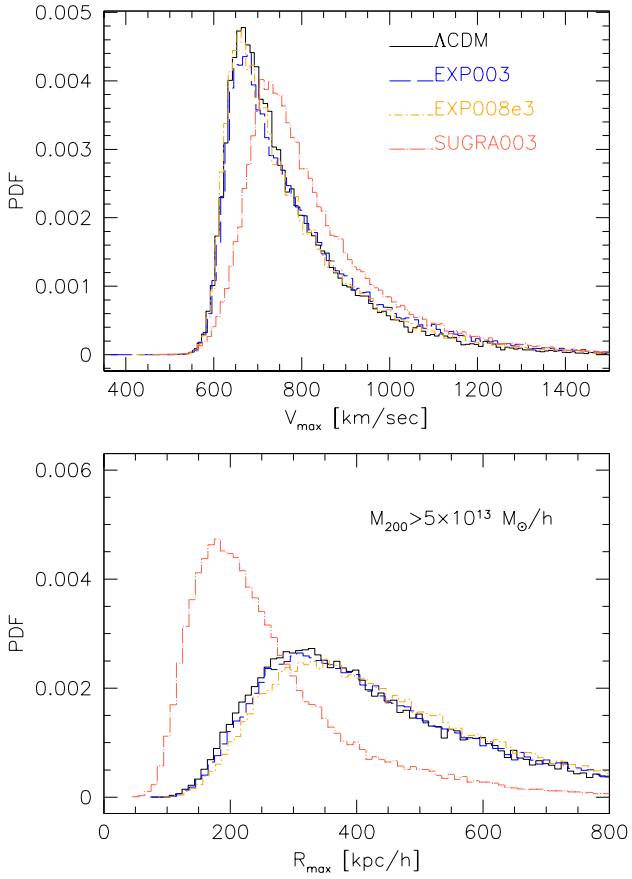

Figure 7. Distribution function of maximum circular velocity (top panel) and of the radius at which this is reached (bottom panel) for all haloes at $z = 0$ with masses larger than $5 \times 10^{13} M_{\odot}/h$ in the four cosmological simulations.

Eq. 20 has the same functional form of the equation proposed by Zhao et al. (2009). These two relations are also overplotted in the other panels. In each panel the gray histograms on the x and the y axis represent the distributions of $t_0/t_{0.5}$ and c_{200}, respectively. The different line types in the EXP003, EXP008e3 and SUGRA panels show the least-squares fit to the corresponding measurements. In Table 3 we summarize these results and give an estimate of the rms of the data points for the different numerical simulation results defined as:

$$\mathrm{rms} = \sqrt{\sum_{i=1}^{N} \frac{(\log(c_i) - \log(c_{model}))^2}{N}}. \qquad (21)$$

Zhao et al. (2009) have shown that the halo concentration has a strong correlation with the time $t_{0.04}$ at which the main halo progenitor assembles 4% its mass, in the idea that typically haloes acquire a concentration of 4 when they assemble 4% of their mass. From their measurements, the best fit relation between the concentration and $t_{0.04}$ reads as:

$$c_{vir} = 4\left[1 + \left(\frac{t_0}{3.75 t_{0.04}}\right)^{8.4}\right]^{1/8}, \qquad (22)$$

where c_{vir} represents the ratio between the scale radius r_s and the virial radius R_{vir}. We recall that Zhao et al. (2009) define R_{vir} such that it encloses an overdensity Δ_{vir} according to the spherical collapse model, with respect to which they also define the virial mass M_{vir}. In Figure 9 we show the median of the correlation between c_{200} and $t_0/t_{0.04}$ for the measurements in the four N-body simulations used in this work. The short-dashed lines show equation (22), that we recall is valid for the c_{vir} and M_{vir} definitions. In the top-left panel the solid line shows our best relation obtained modifying the Zhao et al. (2009) fitting function to be valid for the c_{200} and the M_{200} definitions, which reads as:

$$c_{200} = 4\left[1 + \left(\frac{t_0}{3.2 t_{0.04}}\right)^{8}\right]^{1/13}. \qquad (23)$$

These two curves are also shown in the other three panels of Figure 9. The different curve types in each panel show equation (23) renormalized (see Table 4) in order to best fit the data points. In Table 4 we summarize the results of Figure 9 together with the rms with respect to the different models.

Using the MAH model previously presented in this work and considering the correlations between c_{200} and $t_{0.5}$ and c_{200} and $t_{0.04}$, it is possible to estimate the concentration-mass relation model, in the following way. Given a mass M_{200} at redshift z_0, we can estimate the redshift at which the main halo progenitor assembles half (or 4%) of its mass by using equation (13), and then the corresponding cosmic time by integrating over the scale factor $a = 1/(1+z)$ the inverse of the Hubble constant $1/H(a)$, from which we can obtain c_{200}. In Figure, 10 we show the median of the concentration-mass relation for all haloes more massive than $5 \times 10^{13} M_{\odot}/h$ at redshift $z_0 = 0$. The data points in both right and left panels are the same. In the top panels they represent the median of the concentration-mass relation measured in the ΛCDM simulation, and the shaded region encloses the first and the third quartiles of the distribution at fixed mass. In the bottom panels we show the differences of the median of the measurements in the three cDE models with respect to the ΛCDM one. In Table 5 we summarize the residuals of the $c - M$ estimates with respect to the different model predictions.

Macciò et al. (2008) and Zhao et al. (2009) have shown that haloes in standard ΛCDM simulations with low values of σ_8 and/or Ω_m tend to possess a lower concentration due to their later formation epoch. In what follows we will try to understand if this is also the case in our non-standard cDE simulations, i.e we will enquire whether the concentration can be inferred from the ΛCDM one by simply taking into account the different normalization of the linear matter power spectrum at $z = 0$ within the standard MAH model.

From the analysis presented above, we have already noticed that even if the EXP003 and EXP008e3 models have a higher value of σ_8, the halo concentration is not too different from that measured for haloes of the same mass in the ΛCDM model. Only the SUGRA003 haloes are found to have a significantly higher concentration, irrespectively of their value of σ_8 that is very similar to the one in the ΛCDM run. These results are consistent with the previous findings of Cui et al. (2012).

In order to quantify to what extent halo concentrations are expected to change for different values of σ_8 within a

Table 3. Rms of the data with respect to the models of Figure 8.

model	rms eq. (20)	rms ΛCDM least-squares	rms least-squares	least-square values
ΛCDM	0.128	0.127	-	slope: 0.870, zero point: 0.503
EXP003	0.132	0.134	0.128	0.748, 0.506
EXP008e3	0.133	0.135	0.128	0.749, 0.488
SUGRA003	0.255	0.254	0.135	0.897, 0.704

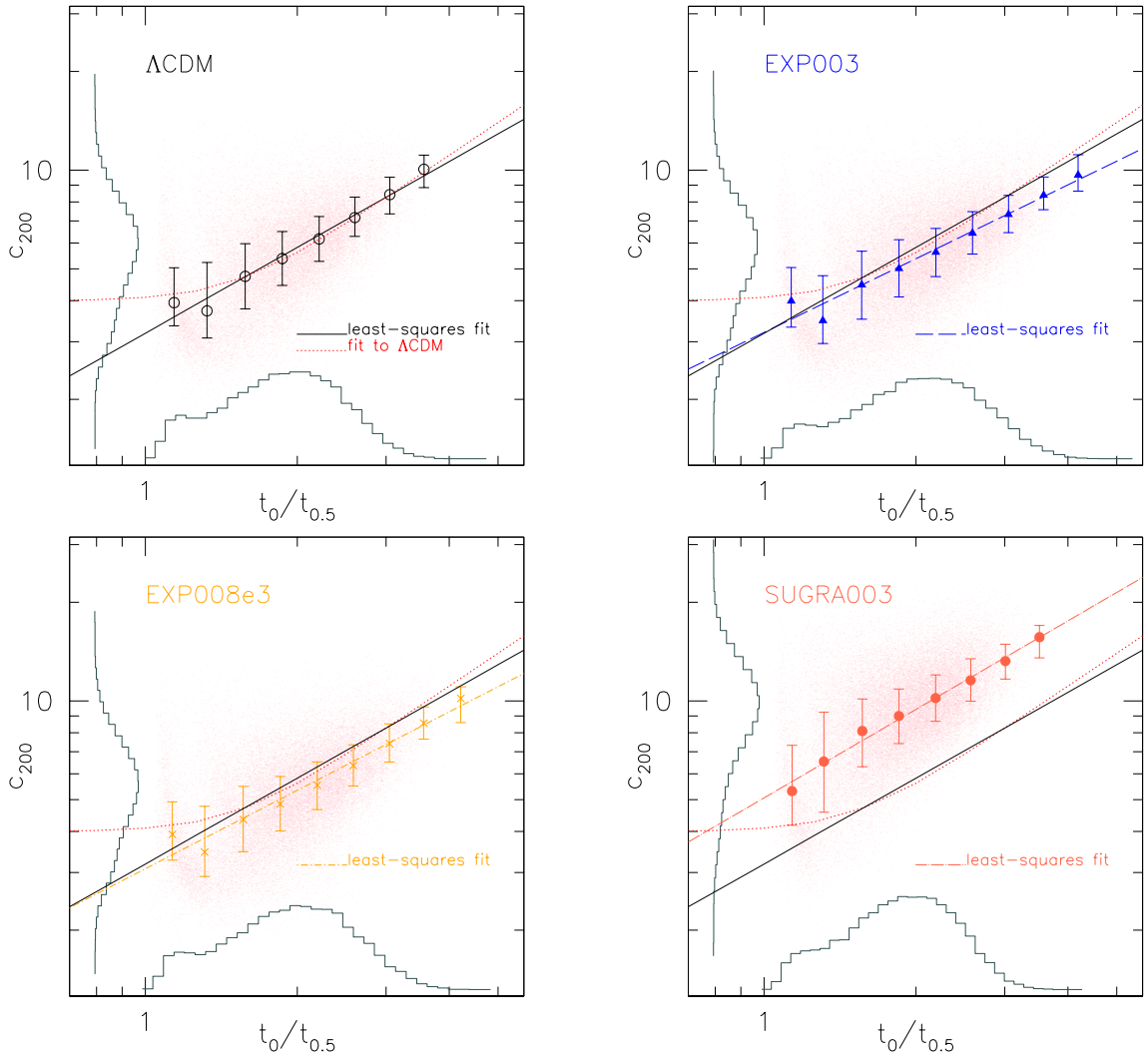

Figure 8. Correlation between the concentration and the formation time when the main halo progenitor assembles 50% of the mass at $z_0 = 0$. The four panels refer to the different cosmological models. In each panel the points with the error bars show the median with the two quartiles. Solid (black) and dotted lines in all panels are the same and represent the least-square fit to the haloes in the ΛCDM simulation and equation (20) respectively. The different line types in the panels referring to the cDE models represent the corresponding least-square fit to their data points.

ΛCDM cosmology, we plot in Figure 11 the concentration-σ_8 prediction combining the least-squares fit $c_{200} - t_0/t_{0.5}$ and the MAH model for a halo with mass $M_{200} = 1 \times 10^{14} M_\odot/h$ as expected for ΛCDM – with the same cosmological parameters of our ΛCDM run – but with different values of σ_8. We take into account the change of σ_8 by renormalizing the mass variance such that:

$$S_{\sigma_8}(M) = \frac{\sigma_8^2}{0.809^2} S_{\Lambda\mathrm{CDM}}(M)\,. \qquad (24)$$

Fixing all the other cosmological parameters, we notice that the larger σ_8 the larger is the halo concentration, as expected, reflecting the fact that haloes tend to form earlier. From the figure we can see that when σ_8 changes from 0.75 to 1 the halo concentration changes by $\sim$ 20%. The data

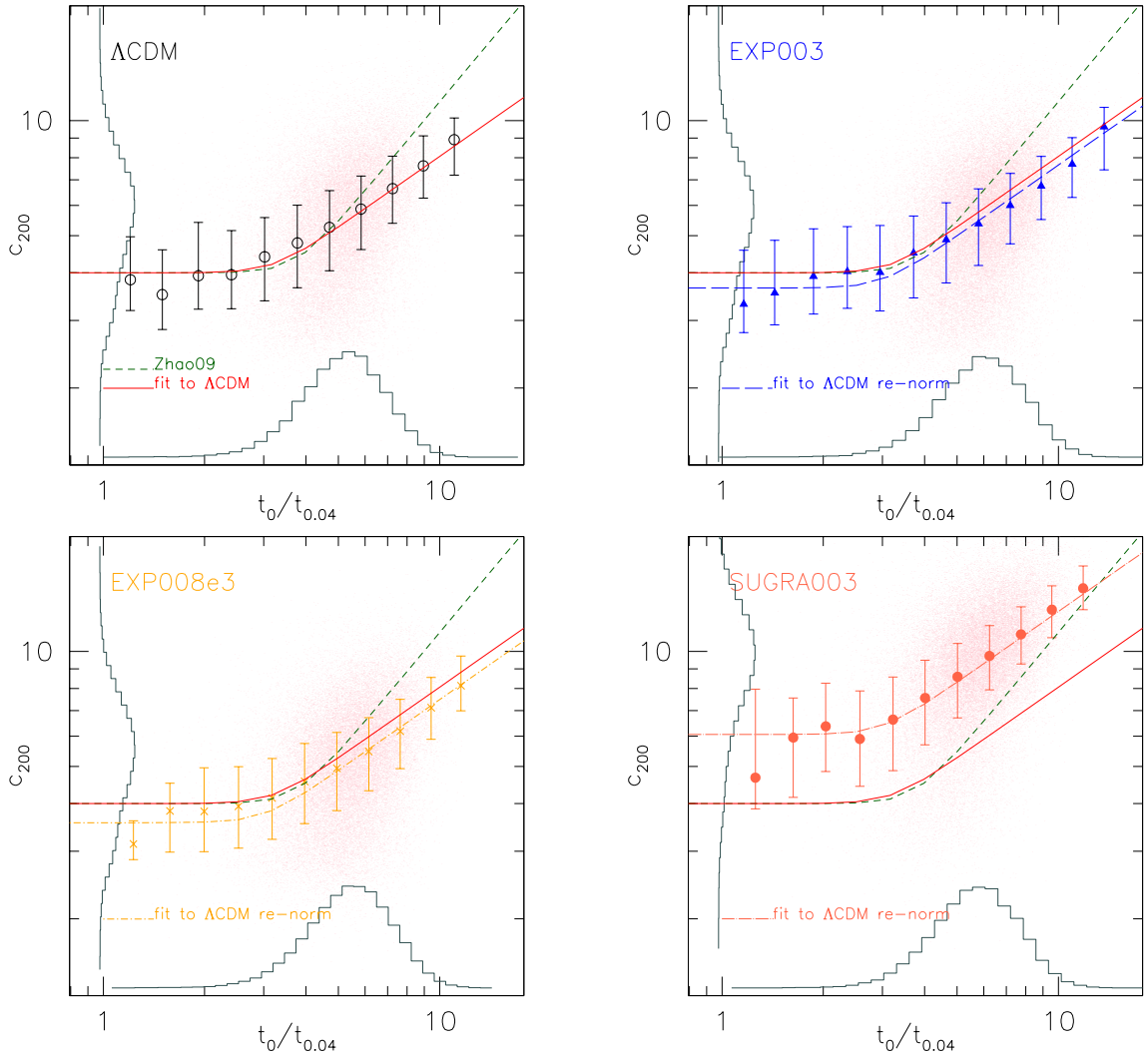

Figure 9. Correlation between the concentration and the formation time when the main halo progenitor assembles 4% of the mass at $z_0 = 0$. Dashed and solid curves in all panels show equations (22) and (23). In the three cDE models the different line type curves show equation (23) renormalized to best fit the corresponding data points.

Table 4. Rms and least-squares fit parameters of the data with respect to the models shown in Figure 9.

model	Zhao et al. (2009)	eq. (23)	eq. (23) renorm.	re-normalization in log space
ΛCDM	0.152	0.143	-	-
EXP003	0.178	0.148	0.143	-0.04
EXP008e3	0.168	0.147	0.143	-0.05
SUGRA003	0.211	0.241	0.143	0.19

Table 5. Rms of the data with respect to the models in the concentration-mass relation, as presented in the panels of Figure 10.

model	from eq. (20)	from l-s c_{200}-$t_0/t_{0.5}$, ΛCDM	from l-s c_{200}-$t_0/t_{0.5}$	from eq. (23)	from eq. (23) renorm.
ΛCDM	0.153	0.154	-	0.154	-
EXP003	0.157	0.161	0.153	0.165	0.154
EXP008e3	0.156	0.161	0.152	0.163	0.151
SUGRA003	0.270	0.259	0.162	0.260	0.162

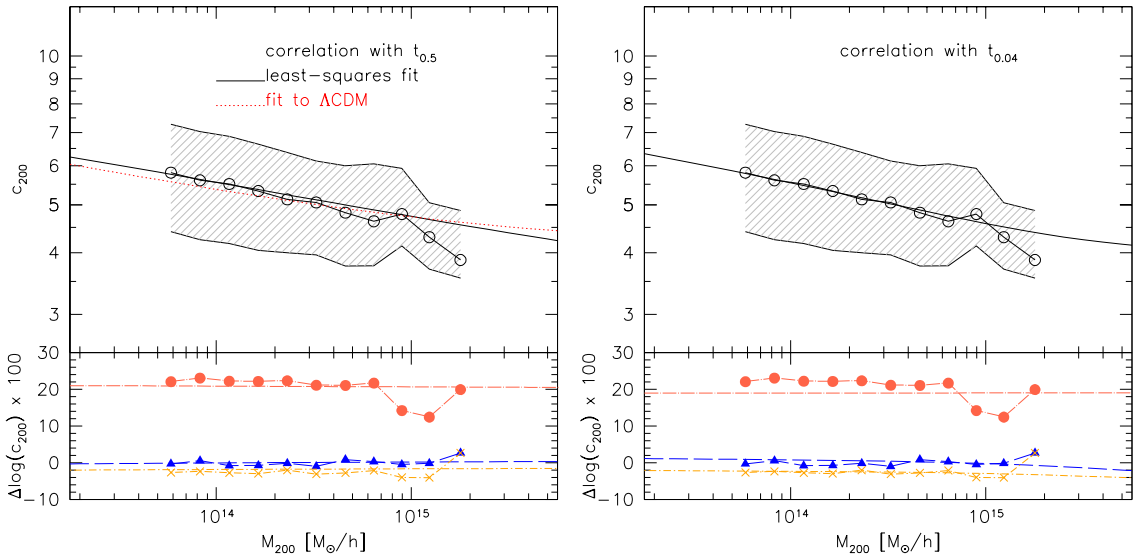

Figure 10. Concentration-mass relation at $z_0 = 0$. The data points show the median $c - M$ relation measured in the ΛCDM simulation and the shaded region encloses the quartiles. In the bottom part of each panel the points show the differences of the $c - M$ measured in the three cDE simulations with respect to the ΛCDM one. In the left-top panel the two solid curves show the $c - M$ prediction using equation (20) and the least-squares relation $c_{200} - t_0/t_{0.5}$. In the bottom left panel the curves show for each model the residuals of the $c - M$ prediction from the least-squares fit in $c_{200} - t_0/t_{0.5}$ relation with respect to the one for ΛCDM. In the top-right panel the $c - M$ prediction is from equation (23) and in the bottom panel the curves are the residuals of the predictions from renormalizing eq. (23).

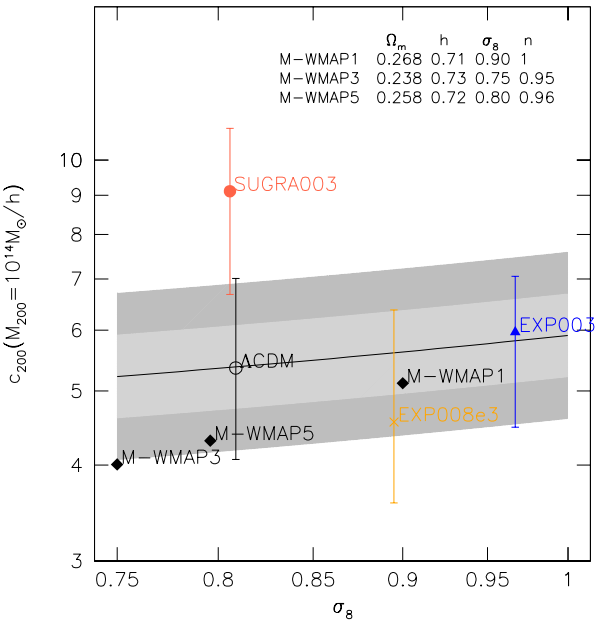

Figure 11. Concentration-σ_8 relation for a halo with mass $M_{200} = 1 \times 10^{14} M_\odot/h$ using the least-squares fit $c_{200} - t_0/t_{0.5}$. The colored data points show the median of the measurements in the simulations with the quartiles. For each simulation, we consider haloes within a logarithmic mass bin $\mathrm{d}\log(M) = 0.001$ centered in $M_{200} = 10^{14} M_\odot/h$. The three black data points labelled as M-WMAP1, M-WMAP3 and M-WMAP5 are the estimates obtained using the best fit relation at $z = 0$ by Macciò et al. (2008) for the three corresponding numerical simulations.

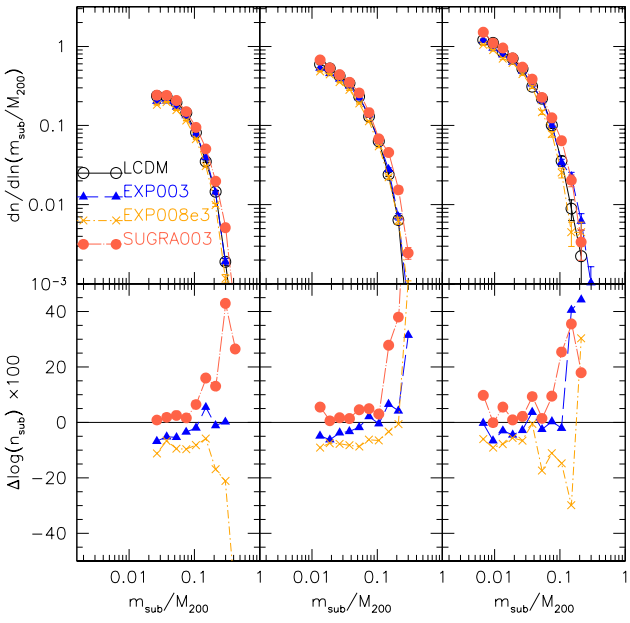

Figure 12. Subhalo mass function measured in the four cosmological simulations used in this work. The subhalo mass is rescaled with respect to the host halo mass M_{200}, and for each halo we have considered only subhaloes with a distance from the host halo centre smaller than R_{200}. In the bottom part of the figure we show the differences of the subhalo mass function with respect to the measurements done in the ΛCDM simulation.

points with the error bars show the median and the quartiles of c_{200} for the same mass haloes measured in the four simulations at $z = 0$; we consider a logarithmic mass bin $\mathrm{d}\log(M) = 0.001$ centered in $M_{200} = 10^{14} M_\odot/h$. The three

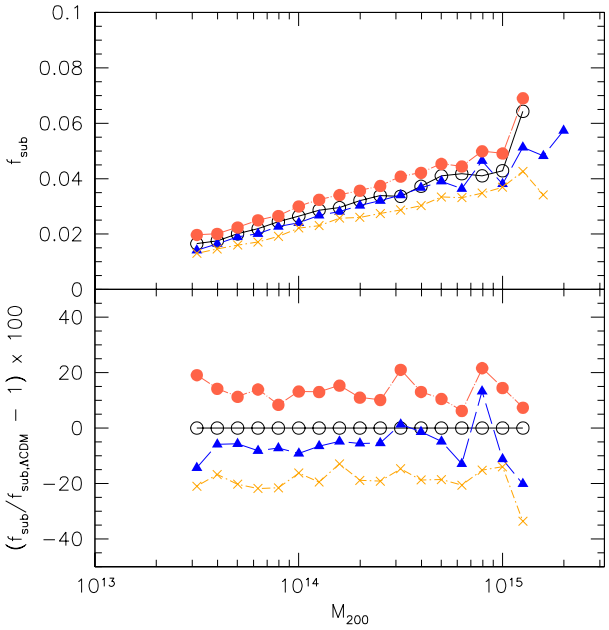

Figure 13. Mass fraction in substructures within R_{200} as a function of the host halo mass. In the bottom part we show the differences of the mass fraction in substructures with respect to the ΛCDM measurements.

data points M-WMAP1, M-WMAP3 and M-WMAP5 are the predictions based on the $c_{200} - M_{200}$ relations by Macciò et al. (2008) for the three cosmological models at $z = 0$. The fact that the predictions from the relations by Macciò et al. (2008) shift down with respect to the solid curve reflects the smaller values for Ω_m adopted their simulations: $\Omega_{m,\Lambda CDM} \gtrsim \Omega_{m,M-WMA1} > \Omega_{m,M-WMA5} > \Omega_{m,M-WMA3}$. From the figure we notice that haloes in EXP003 possess a higher concentration than in ΛCDM, consistently with the higher value of $\sigma_8(z_0)$ that characterizes the model (see Table 1).

However, the expected trend of c_{200} as a function of σ_8 is not followed both in EXP008e3 and SUGRA003. This point represents a central result of the present work, and deserves a more detailed discussion. It is well known that standard cDE models are characterized by a suppression of the non-linear matter power spectrum with respect to what ΛCDM predicts for any given value of σ_8. This has been demonstrated both by running cDE N-body simulations with the same σ_8 (as done e.g. in Baldi 2011a) and by comparing the non-linear matter power spectrum extracted from cDE N-body simulations normalized at $z_{\rm CMB} \approx 1100$ to the predictions of HALOFIT (Smith et al. 2003) for the corresponding values of σ_8 (see e.g. Baldi 2012b). Such suppression is determined by the action of the "friction term" (see the discussion in Section 3 above) that for standard cDE models has the effect of suppressing the growth of nonlinear structures. Correspondingly, for a fixed value of σ_8 CDM haloes are found to be less concentrated in a cDE cosmology when compared with respect to ΛCDM (see e.g. Baldi et al. 2010a; Baldi 2011a; Li & Barrow 2011). For more complex cDE models, like time-dependent couplings or the "bouncing" cDE scenario, the role played by the "friction term" is not so straightforward as the latter can change sign during the cosmic evolution or have a non-trivial interplay with the time evolution of the coupling itself. In such more general scenarios, halo concentrations at fixed σ_8 can be both higher and lower than in ΛCDM, depending on the specific model.

Among the models considered in the present work, the slight increase of halo concentrations for the standard EXP003 cDE model shows how the suppression associated to the "friction term" is compensated by the higher value of σ_8 of this cosmological model as compared to ΛCDM. Furthermore, the lower and higher values of halo concentrations with respect to what is predicted by the standard ΛCDM scenario, that are observed for the EXP008e3 and SUGRA003 models, respectively, show how the dynamical evolution of the DE scalar field can alter the structural properties of CDM haloes in a way that is clearly independent of the evolution of linear density perturbations. For instance, in the case of the "bouncing" cDE model (SUGRA003), halo concentrations significantly grow in time at low redshifts (as already found by Cui et al. 2012) due to the particular dynamics of the DE scalar field that inverts its direction of motion at $z_{\rm inv} \simeq 6.8$ thereby also changing the sign of the "friction" term $\beta_c\dot{\phi}$ (see Baldi 2012a, for a more detailed discussion of the dynamics of "bouncing" cDE). The latter then acts as a dissipation term for virialized objects inducing an adiabatic contraction of halos that consequently evolve towards more concentrated virial configurations.

This direct relation between the dynamics of the underlying DE field and the formation and evolution of nonlinear structures offers the interesting prospect of using the formation history of CDM haloes and their structural properties to disentangle cDE effects from possible variations of cosmological parameters (as e.g. σ_8), of the linear galaxy bias, and of the mass of cosmic neutrinos (see e.g. La Vacca et al. 2009; Marulli et al. 2011).

6.2 Halo substructures

Studying the subhalo population in DM haloes extracted from a standard cosmological ΛCDM simulation at $z = 0$, Giocoli et al. (2010a) found that more concentrated haloes, forming at higher redshift, tend to possess on average less substructures above the same minimum mass. They have also stressed the fact that considering haloes with the same mass, the ones that form earlier not only possess a higher concentration, but also less subhaloes. This is because halo progenitors are accreted earlier, then spending more time in the potential well of the host halo, and thereby tend to lose a larger fraction of their initial mass (van den Bosch et al. 2005; Giocoli et al. 2008). To see if this phenomenology is also reflected in the cDE simulations considered in this work, we plot in Figure 12 the subhalo mass function considering for each halo all substructures resolved by SUBFIND with a distance from the host halo centre smaller than R_{200}. In the top part of the figure we show the subhalo mass function for three different host halo mass bin (as in Figure 5) at $z = 0$, while in the bottom one the differences with respect to the measurements in the ΛCDM simulation. Since we have shown that haloes in SUGRA assemble earlier and are more concentrated than those in the ΛCDM run, we would have expected them to possess less substructures, on the contrary to what is shown in the figure. Also the subhalo population in the EXP003 and EXP008e3 cosmologies does not reflect their mass accretion history. In

these models, haloes possess less substructures than those in ΛCDM since they form earlier, but even if in EXP003 haloes form earlier than those in EXP008e3 they are still found to host more substructures than in the latter model. This statement is further demonstrated in Figure 13 where we show the halo mass fraction in subhaloes as a function of M_{200}. In the bottom part of the figure we show again the differences of the measurements in the cDE with respecto to the one in ΛCDM: haloes in SUGRA (EXP008e3) are more (less) substructured than those in ΛCDM by $\sim 15\%$ while the difference between EXP003 and ΛCDM is only of the order of a few percent. We argue that the main reason why SUGRA003 (EXP008e3) possesses more (less) substructures at $z = 0$ is that halo progenitors at any redshift $z < 1$, which end up in present-day substructures, are more (less) concentrated than in ΛCDM; so the gravitational heating and tidal stripping are less (more) efficient in disrupting the satellites.

7 SUMMARY AND CONCLUSIONS

Using state-of-the-art cosmological simulations for cDE models from the CoDECS Project we have studied how collapsed haloes grow as a function of the cosmic time, and how present-day systems acquire their structural properties. We summarize our study and main results as follows.

• We updated the model developed by Giocoli et al. (2012b) in the context of the extended-Press & Schechter (1974) formalism to be able to describe the halo mass accretion history of a ΛCDM cosmology when haloes are identified by their M_{200} mass (instead of M_{vir}), defined as the mass of the spherical region around the halo center enclosing an average density 200 times larger than the critical density of the Universe.

• By rescaling the MAH model with the normalization of the linear matter power spectrum for the different cDE runs, we noticed that the simulation results are reproduced quite well for small masses and low redshift. For galaxy cluster-size haloes and up to high redshifts, when less than 1% of the present-day mass is assembled, the models and the simulation measurements differ by about 20%. Haloes at $z = 0$ in the different cDE cosmologies (standard cDE, time-dependent cDE, and "bouncing" cDE) typically assemble their mass at higher redshift as compared to those in the standard ΛCDM run.

• We studied the formation redshift z_f for different fractions f of the assembled mass: standard and time-dependent cDE show a systematically higher z_f by ~ 20 and $\sim 10\%$, respectively, as compared to ΛCDM. On the other hand haloes in our "bouncing" cDE cosmology have a formation redshift quite similar to those in ΛCDM, for small f, while for large assembled fractions z_f can also be higher than in ΛCDM by up to $\sim 20\%$.

• Analyzing the correlation between the halo concentration and two typical formation times $t_{0.5}$ and $t_{0.04}$, we confirm that the usual correlation between halo formation time and halo concentration at $z = 0$ (the earlier the formation time, the higher the concentration) still holds in cDE cosmologies. Generalizing the prediction for ΛCDM we provide some fitting functions for such correlations also in cDE models. In particular, in our "bouncing" cDE scenario haloes are very concentrated at $z = 0$, inconsistently with the correlation expected for standard cosmologies (Cui et al. 2012). Such structural properties could produce very compact and luminous galaxies located in the centre of haloes and also galaxy clusters that are very efficient for strong lensing.

• Considering the correlation between c_{200} and the time at which the main halo progenitor assembles half of its mass, we have confirmed that for standard ΛCDM cosmologies the concentration is a monotonic function of σ_8: in particular for a cluster-size halo the change in concentration between two ΛCDM cosmologies with $\sigma_8 = 0.75$ and $\sigma_8 = 1$ is of about 20%. Moving to cDE cosmologies, we have shown that only the standard cDE run, characterized by an exponential self-interaction potential and a constant coupling, is found to be in agreement with such predictions, while both cDE models with a time-dependent coupling and the "bouncing" cDE model are not found to be consistent with the expected evolution of halo concentrations with σ_8. This inconsistency offers the interesting prospect of disentangling the effects of dark interactions from the variation of standard cosmological parameters using the evolution of halo concentrations (Giocoli et al. 2012c).

• The standard mass accretion history model is also found to be not directly applicable to predict the subhalo population of the host haloes at $z = 0$ within cDE cosmologies. In fact, if we generalize to the cDE simulations the statements by Gao et al. (2004), van den Bosch et al. (2005), and Giocoli et al. (2008) - valid for standard ΛCDM - that haloes with a higher formation redshift typically possess less substructures, we would expect to find more substructures in ΛCDM than in all our cDE models at any fixed halo mass. On the contrary, we find that the trend is actually reversed, with haloes of the same mass having $\sim 15\%$ more substructures within R_{200} in the "bouncing" cDE run than in ΛCDM, while haloes forming within a time-dependent cDE cosmology have less substructures by the same amount, while haloes in standard cDE are roughly consistent with their higher formation redshift and concentration but have slightly less substructures then in ΛCDM. We argue that the higher concentration and the larger number of clumps in the SUGRA003 model are due to the fact haloes formed when the average density of the universe was larger, and the difference in the average density between the formation time of the small halos and the larger ones was also larger than in the in ΛCDM. This makes satellites not only more concentrated than in thoes in ΛCDM, but also more concentrated relative to the host halos: the subhalos then tend to survive tidal striping for longer time. In summary, while in standard ΛCDM simulation – indepdentently of the small scale behavior of the linear power spectrum used to generate the initial conditions (Schneider et al. 2012) – the concentration-mass relation is expected to prove the halo formation time, the subhalo abundance as a function of the host halo mass validate the dynamical friction and the tidal stripping (van den Bosch et al. 2005).

To conclude, in the present work we have performed a detailed analysis of the mass accretion history of collapsed haloes in a sample of coupled Dark Energy cosmologies including different choices of the Dark Energy self-interaction

and coupling functions. We have studied how haloes acquire their structural properties along the cosmic time and tested whether it is possible to attribute the detected differences with respect to the standard ΛCDM case to the different linear power spectrum normalization. Interestingly, we found that this is not possible for all coupled Dark Energy models, and we identified which observables allow to break such a degeneracy. Finally, we have investigated by how much halo concentration and subhalo abundance deviate from ΛCDM for the three coupled Dark Energy models included in our simulations set. In particular, we showed that the unexpected high concentration and clumpiness of haloes make the "bouncing" coupled Dark Energy model particularly interesting in the context of both weak and strong gravitational lensing. We intend to study the possibility of distinguishing such models from ΛCDM using lensing data in future work.

APPENDIX A: MASS ACCRETION HISTORY IN TERMS OF THE VIRIAL MASS FOR THE ΛCDM SIMULATION

In this Appendix we show that the MAH model built following back in time the haloes in the ΛCDM simulation in terms of their virial mass M_{vir} is in perfect agreement with the results obtained by Giocoli et al. (2012b). In Figure A1 we show the cumulative generalized formation redshift distribution when 90%, 50%, 10% and 1% of the halo mass is assembled in term of the universal variable w_f. We compute the redshift at which the main halo progenitor assembles a fraction f of its mass at $z = 0$ interpolating its mass accretion history along the different simulation snapshots, and then compute $w_f = (\delta_c(z_f) - \delta_c(z_0))/\sqrt{S(fM_{vir}) - S(M_{vir})}$. The solid line in the figure shows equation (12) with the best fit value of α_f. The dashed curve refers to the relation by Nusser & Sheth (1999) modified as proposed by Giocoli et al. (2007) and the dot-dashed curve equation (12) with the $\alpha_f - f$ relation by Giocoli et al. (2012b). We notice that our best fit is in very good agreement with what found by Giocoli et al. (2012b), and does not depend on the different cosmological parameters of the simulation since w_f is a universal variable (Press & Schechter 1974; Bond et al. 1991; Lacey & Cole 1993, 1994). The small differences can be traced back to the different code used to run the two numerical simulations and to do the post processing analyses. While HYDRA (Couchman et al. 1995) and GADGET (Springel et al. 2001a) have been used for the GIF2 simulation studied by Giocoli et al. (2012b), a modified version of GADGET2 (Springel 2005) developed to include all the additional physical effects that characterize cDE models (Baldi et al. 2010b) has been run four our ΛCDM simulation. For the post-processing analyses Giocoli et al. (2012b) have adapted and run the pipeline presented by Tormen et al. (2004), while here we have run the codes by Springel et al. (2001a) and Boylan-Kolchin et al. (2009). We recall the reader also on the fact that the GIF2 is a pure DM simulation while the CoDECS presents a baryon fluid with no hydrodynamic treatment included.

In Figure A2 we show the correlation between the free parameter of the MAH model α_f and the assembled mass fraction. The data points represent the best fit values obtained fitting the cumulative formation redshift distribution for different values of f; the shaded region encloses 1σ and 2σ contours around them. In the figure, the solid curve represents the following relation:

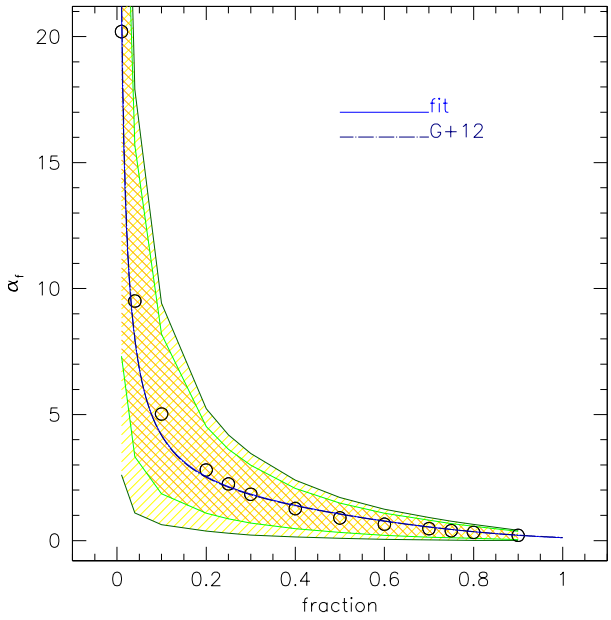

Figure A2. As Figure 3 but in terms of M_{vir}.

$$\alpha_f = \frac{0.837}{f^{0.7}}\, e^{-2f^3}, \quad \text{(A1)}$$

while the dot-dashed one is for:

$$\alpha_f = \frac{0.815}{f^{0.707}}\, e^{-2f^3}, \quad \text{(A2)}$$

as found by Giocoli et al. (2012b). The two relations for the ΛCDM runs are in perfect agreement confirming the fact that the MAH model can be generalized for any ΛCDM cosmology, independently of the cosmological parameters.

APPENDIX B: PUBLICLY AVAILABLE MERGER TREE FILES ON THE CODECS DATABASE

The merger trees of the different L-CoDECS simulations used to perform the analysis discussed in the present paper have been produced using a linking algorithm outlined in Springel et al. (2005) and Springel et al. (2008). With such algorithm, we produced a single merger tree file for each cosmological model of the L-CoDECS suite (i.e. even for those models that have not been considered in the present paper).

As an extension of the public CoDECS database, we hereby release the merger tree files that are now directly available at the CoDECS website (http://www.marcobaldi.it/CoDECS). These are unformatted binary files with an average size of about 10 Gb, and detailed instructions on how to read and use the data can be found on the CoDECS guide (version 2.0) that can also be directly downloaded from the CoDECS website.

The access to these files is subject to the same terms of use that apply to the whole CoDECS public database.

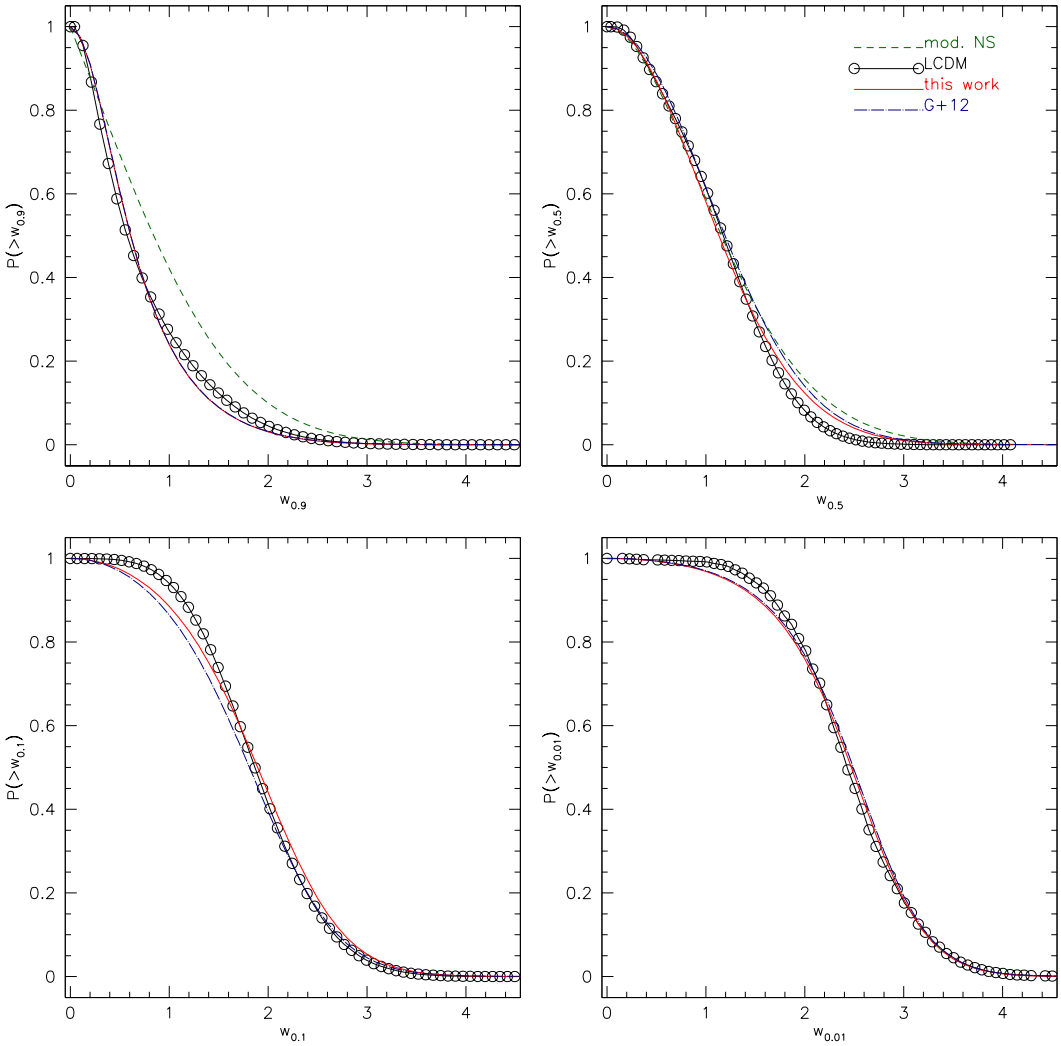

Figure A1. As Figure 2 but in terms of M_{vir}.

ACKNOWLEDGMENTS

We are grateful to Giuseppe Tormen and Ravi K. Sheth for their comments and suggestions.

CG and RBM's research is part of the project GLENCO, funded under the European Seventh Framework Programme, Ideas, Grant Agreement n. 259349. MB is supported by the Marie Curie Intra European Fellowship "SIDUN" within the 7th European Community Framework Programme and also acknowledges support by the DFG Cluster of Excellence "Origin and Structure of the Universe" and by the TRR33 Transregio Collaborative Research Network on the "DarkUniverse". We acknowledge the support from grants ASI-INAF I/023/12/0, PRIN MIUR 2010-2011 "The dark Universe and the cosmic evolution of baryons: from current surveys to Euclid".

REFERENCES

Amendola L., 2000, Phys. Rev., D62, 043511
Amendola L., 2004, Phys. Rev., D69, 103524
Amendola L., Appleby S., Bacon D., et al., 2012, ArXiv e-prints
Amendola L., Baldi M., Wetterich C., 2008, Phys.Rev.D, 78, 2, 023015
Baldi M., 2011a, MNRAS, 414, 116
Baldi M., 2011b, MNRAS, 411, 1077
Baldi M., 2012a, MNRAS, 420, 430
Baldi M., 2012b, MNRAS, 422, 1028
Baldi M., Pettorino V., Robbers G., Springel V., 2010a, MNRAS, 403, 1684
Baldi M., Pettorino V., Robbers G., Springel V., 2010b, MNRAS, 403, 1684
Bartelmann M., Schneider P., 2001, Physics Reports, 340, 291
Bertotti B., Iess L., Tortora P., 2003, Nature, 425, 374
Beynon E., Baldi M., Bacon D. J., Koyama K., Sabiu C., 2012, Mon.Not.Roy.Astron.Soc., 422, 3546
Bond J. R., Cole S., Efstathiou G., Kaiser N., 1991, ApJ, 379, 440
Boylan-Kolchin M., Springel V., White S. D. M., Jenkins A., Lemson G., 2009, MNRAS, 398, 1150
Brax P., Martin J., 1999, Phys. Lett., B468, 40

Bryan G. L., Norman M. L., 1998, ApJ, 495, 80
Bullock J. S., Kolatt T. S., Sigad Y., et al., 2001, MNRAS, 321, 559
Cacciato M., Lahav O., van den Bosch F. C., Hoekstra H., Dekel A., 2012, MNRAS, 426, 566
Caldera-Cabral G., Maartens R., Urena-Lopez L. A., 2009, Phys. Rev., D79, 063518
Cooray A., Sheth R., 2002, Physics Reports, 372, 1
Couchman H. M. P., Thomas P. A., Pearce F. R., 1995, ApJ, 452, 797
Cui W., Baldi M., Borgani S., 2012, MNRAS, 424, 993
Damour T., Gibbons G. W., Gundlach C., 1990, Phys. Rev. Lett., 64, 123
Davis M., Efstathiou G., Frenk C. S., White S. D. M., 1985, ApJ, 292, 371
De Boni C., Ettori S., Dolag K., Moscardini L., 2012, MNRAS, 218
De Felice A., Tsujikawa S., 2010, Living Rev.Rel., 13, 3
De Lucia G., Kauffmann G., Springel V., et al., 2004, MNRAS, 348, 333
Despali G., Tormen G., Sheth R. K., 2012, ArXiv e-prints
Eke V. R., Cole S., Frenk C. S., 1996, MNRAS, 282, 263
Farrar G. R., Peebles P. J. E., 2004, ApJ, 604, 1
Frenk C. S., White S. D. M., Davis M., 1983, ApJ, 271, 417
Frenk C. S., White S. D. M., Efstathiou G., Davis M., 1990, ApJ, 351, 10
Gao L., Navarro J. F., Cole S., et al., 2008, MNRAS, 387, 536
Gao L., White S. D. M., 2007, MNRAS, 377, L5
Gao L., White S. D. M., Jenkins A., Stoehr F., Springel V., 2004, MNRAS, 355, 819
Giocoli C., Bartelmann M., Sheth R. K., Cacciato M., 2010, MNRAS, 408, 300
Giocoli C., Meneghetti M., Bartelmann M., Moscardini L., Boldrin M., 2012a, MNRAS, 421, 3343
Giocoli C., Meneghetti M., Ettori S., Moscardini L., 2012c, MNRAS, 426, 1558
Giocoli C., Moreno J., Sheth R. K., Tormen G., 2007, MNRAS, 376, 977
Giocoli C., Tormen G., Sheth R. K., 2012b, MNRAS, 422, 185
Giocoli C., Tormen G., Sheth R. K., van den Bosch F. C., 2010a, MNRAS, 404, 502
Giocoli C., Tormen G., van den Bosch F. C., 2008, MNRAS, 386, 2135
Komatsu E., et al., 2011, Astrophys. J. Suppl., 192, 18
Koyama K., Maartens R., Song Y.-S., 2009, JCAP, 0910, 017
La Vacca G., Kristiansen J. R., Colombo L. P. L., Mainini R., Bonometto S. A., 2009, JCAP, 0904, 007
Lacey C., Cole S., 1993, MNRAS, 262, 627
Lacey C., Cole S., 1994, MNRAS, 271, 676
Lee J., Baldi M., 2011, ApJ in press, arXiv:1110.0015, ApJ Submitted
Li B., Barrow J. D., 2011, Phys. Rev., D83, 024007
Li Y., Mo H. J., Gao L., 2008, MNRAS, 389, 1419
Lucchin F., Matarrese S., 1985, Phys. Rev., D32, 1316
Lukić Z., Reed D., Habib S., Heitmann K., 2009, ApJ, 692, 217
Macciò A. V., Dutton A. A., van den Bosch F. C., 2008, MNRAS, 391, 1940
Macciò A. V., Dutton A. A., van den Bosch F. C., Moore B., Potter D., Stadel J., 2007, MNRAS, 378, 55
Marulli F., Baldi M., Moscardini L., 2012, MNRAS, 420, 2377
Marulli F., Carbone C., Viel M., Moscardini L., Cimatti A., 2011, MNRAS, 418, 346
Moster B. P., Somerville R. S., Maulbetsch C., et al., 2010, ApJ, 710, 903
Nakamura T. T., Suto Y., 1997, Progress of Theoretical Physics, 97, 49
Navarro J. F., Frenk C. S., White S. D. M., 1997, ApJ, 490, 493
Neto A. F., Gao L., Bett P., et al., 2007, MNRAS, 381, 1450
Nusser A., Sheth R. K., 1999, MNRAS, 303, 685
Pace F., Waizmann J.-C., Bartelmann M., 2010, MNRAS, 406, 1865
Perlmutter S., et al., 1999, Astrophys. J., 517, 565
Press W. H., Schechter P., 1974, ApJ, 187, 425
Ratra B., Peebles P. J. E., 1988, Phys. Rev., D37, 3406
Riess A. G., et al., 1998, Astron. J., 116, 1009
Schmidt B. P., et al., 1998, Astrophys.J., 507, 46
Schneider A., Smith R. E., Macciò A. V., Moore B., 2012, MNRAS, 424, 684
Seljak U., 2000, MNRAS, 318, 203
Shen Y., Hennawi J. F., Shankar F., et al., 2010, ApJ, 719, 1693
Sheth R. K., Tormen G., 1999, MNRAS, 308, 119
Sheth R. K., Tormen G., 2002, MNRAS, 329, 61
Sheth R. K., Tormen G., 2004, MNRAS, 349, 1464
Smith R. E., et al., 2003, Mon. Not. Roy. Astron. Soc., 341, 1311
Springel V., 2005, MNRAS, 364, 1105
Springel V., et al., 2005, Nature, 435, 629
Springel V., Wang J., Vogelsberger M., et al., 2008, MNRAS, 391, 1685
Springel V., White S. D. M., Jenkins A., et al., 2005, Nature, 435, 629
Springel V., White S. D. M., Tormen G., Kauffmann G., 2001b, MNRAS, 328, 726
Springel V., Yoshida N., White S. D. M., 2001a, New Astronomy, 6, 79
Tarrant E. R. M., van de Bruck C., Copeland E. J., Green A. M., 2012, Phys.Rev.D, 85, 2, 023503
Tormen G., Moscardini L., Yoshida N., 2004, MNRAS, 350, 1397
Tsujikawa S., 2010, arXiv:1004.1493
van den Bosch F. C., 2002, MNRAS, 331, 98
van den Bosch F. C., Tormen G., Giocoli C., 2005, MNRAS, 359, 1029
Vera Cervantes D. V., Marulli F., Moscardini L., Baldi M., Cimatti A., 2012, ArXiv e-prints
Wetterich C., 1988, Nucl. Phys., B302, 668
Wetterich C., 1995, Astron. Astrophys., 301, 321
Wetterich C., 2007, Phys. Lett., B655, 201
White S. D. M., 1988, in NATO ASIC Proc. 219: The Early Universe, edited by W. G. Unruh, G. W. Semenoff, 239–260
White S. D. M., Rees M. J., 1978, MNRAS, 183, 341
Will C. M., 2005, Living Rev.Rel., 9, 3
Zhao D. H., Jing Y. P., Mo H. J., Bnörner G., 2009, ApJ, 707, 354